

Conformationally Averaged Score Functions for Electronic Propagation in Proteins

Tsutomu Kawatsu,^{*,†,||} David N. Beratan,^{*,†,‡} and Toshiaki Kakitani[§]

Department of Chemistry, Duke University, Durham, North Carolina 27708, Department of Biochemistry, Duke University Medical Center, Durham, North Carolina 27708, and Department of General Education, Faculty of Science and Technology, Mejo University, Tempaku, Nagoya 468-8502, Japan

Received: April 27, 2005; In Final Form: December 30, 2005

We explore the influence of conformational dynamics on protein-mediated electron donor–acceptor interactions. We introduce a thermally averaged score function to characterize electronic propagation from redox cofactors into the protein and solvent. The score function is explored for myoglobin at the extended-Hückel level, and the results are compared with those of simpler models. The conformationally averaged quantum results are consistent with the empirical analysis of the *Pathways* model. Notably, subtle effects of quantum interference among multiple coupling pathways that arise in static structures are largely averaged out when protein thermal motion is included. Propagation through bulk water near the single-protein interface decays rapidly with distance.

1. Introduction

A central challenge in describing biological electron transfer (ET) is to understand under what circumstances simplifications and approximations may be used to describe the electron-tunneling processes. Thermal fluctuations in proteins and in the surrounding solvent are known to cause large (order of magnitude) variations in donor–acceptor tunneling interactions.^{1–8} Their effects are particularly important when multiple interfering coupling pathways facilitate donor–acceptor interactions. The coupling element, T_{DA} , enters the nonadiabatic ET rate through^{9,10}

$$k_{\text{ET}} = \frac{2\pi}{\hbar} |T_{\text{DA}}|^2 (\text{FC}) \quad (1)$$

Coupling interactions can vary strongly with the thermal motion of the protein structure.^{1,2,5–8} Destructive interference among multiple coupling pathways^{1,2,8} can decrease $|T_{\text{DA}}|$ dramatically for some structures. Despite these fluctuations, the Condon approximation appears to remain valid for ET through proteins because the structure fluctuations are slow on the time scale of reaction coordinate motion in the curve-crossing region.⁷ When bridge fluctuations are rapid on the ET time scale, the mean-square coupling $\langle |T_{\text{DA}}|^2 \rangle$ appears in eq 1 in place of $|T_{\text{DA}}|^2$.^{1–3,5,7}

Our aim here is to compare predictions of T_{DA} and $\langle |T_{\text{DA}}|^2 \rangle^{1/2}$ that arise from increasingly fine-grained models of the tunneling process.^{4,11,12} The position of the donors and acceptors can be varied experimentally and may be controlled. As such, a score function that predicts $\langle |T_{\text{DA}}|^2 \rangle^{1/2}$ values may prove to be useful. Here, we introduce a conformationally averaged score function that measures the magnitude of the electronic propagation from the donor orbitals throughout the bridge. The score function is computed using the protein's green function and a perturbation theory description of donor–protein and protein–acceptor

interactions. We explore the score function for the protein surface atoms (Figure 11a). The score is also extended into surrounding water. We characterize the conformationally averaged score for myoglobin (section 3), and we compare the extended-Hückel level score function with the *Pathways*-level analysis (section 4).

T_{DA} values in proteins can be estimated using a range of models. The simplest description treats the protein as a wide one-dimensional square barrier^{13–18}

$$T_{\text{DA}} = T_0 \exp(-\beta R_{\text{DA}}/2) \quad (2)$$

R_{DA} is the donor–acceptor distance. T_0 depends on the cofactors.¹⁹ *Pathways* analysis, a finer-grained model, suggests that β varies with protein structure.^{20–25} The *Pathways* model assumes that T_{DA} is approximated by a product of decay factors characteristic of the medium connectivity

$$T_{\text{DA}} = b \text{Max} \left\{ \prod_{i=1}^{N-1} \epsilon_{i,i+1}^{\text{X}}(r_{i,i+1}) \right\} \quad (3)$$

b depends on the donor/acceptor cofactors and their interactions with the protein. i indexes atoms on the strongest coupling pathway. X = C, H, S indicates covalent bonds, hydrogen bonds, or nonbonded (through-space) interactions associated with the $i \rightarrow i+1$ interaction. $r_{i,i+1}$ is the distance between atoms i and $i+1$. $\epsilon_{i,i+1}^{\text{X}}$ is an empirical decay factor for electronic coupling between atoms i and $i+1$. This expression for the coupling is motivated by two facts: (1) Tunneling decay in periodic potentials adopts a simple product form; (2) tunneling in the perturbative regime adopts a product form, although each ϵ value need not be equal.¹⁹ The decay factors $\epsilon_{i,i+1}^{\text{X}}(r_{i,i+1})$ are often approximated by

$$\epsilon_{i,i+1}^{\text{X}}(r_{i,i+1}) = \begin{cases} \epsilon_{\text{B}} & (\text{X} = \text{C}) \\ \epsilon_{\text{B}}^2 \exp(-\beta_{\text{s}}(r_{i,i+1} - 2R_{\text{c}})) & (\text{X} = \text{H}) \\ \epsilon_{\text{B}} \exp(-\beta_{\text{s}}(r_{i,i+1} - R_{\text{c}})) & (\text{X} = \text{S}) \end{cases} \quad (4)$$

$\epsilon_{\text{B}} = 0.6$, $R_{\text{c}} = 1.4 \text{ \AA}$, and $\beta_{\text{s}} = 1.7 \text{ \AA}^{-1}$ are used for organic

* Authors to whom correspondence should be addressed. E-mail: tsutomu.kawatsu@duke.edu; david.beratan@duke.edu.

† Duke University.

‡ Duke University Medical Center.

§ Mejo University.

|| Current address: Department of Chemistry and Biochemistry, Georgia Institute of Technology, 770 State St., Atlanta, GA 30332.

molecules. A smaller value for β_s was also suggested recently.²⁶ *Pathways* analysis indicates that a tube of atoms surrounding the single “strongest” coupling pathway controls the donor–acceptor interaction,^{20–22} and metrics to assess atom and group contributions to T_{DA} have been developed.^{24,25,27–39} For bimolecular ET, surface scoring functions help determine viable ET-active docking geometries.^{34–39} Most scoring analysis assumes that the molecular structure is fixed. The *Pathways* model itself defines a score for each residue in a protein. The scoring function indicates the electronic coupling for a pathway linking atom $i = 1$ and j . We call this value the “pathway amplitude” (PA)^{24,25,36}

$$PA_j \equiv b_D \prod_{i=1}^j \epsilon_{i,i+1}^X(r_{i,i+1}) \quad (5)$$

b_D is added here as a unitless scaling factor to describe amplitude decay between the donor and the first step of the pathway, to connect with the quantum scoring function. Switching D to A in eq 5, PA_j (for rigid geometries) describes propagation of the hole from the acceptor. Protein surface maps of PA_j have been used to analyze interprotein interactions and ET.^{34–39} Packing density analysis¹⁴ is nearly identical.²⁶ T_{DA} can also be computed using semiempirical^{17,40–44} or ab initio^{12,18} quantum chemical methods that include pathway interferences in an explicit manner. Quantum methods predict coupling pathway structure in qualitative agreement with *Pathways* analysis.²⁷

The value of T_{DA} computed perturbatively in the donor-bridge and acceptor-bridge interactions is^{19,43–45}

$$T_{DA} = a_D a_A \mathbf{D} \mathbf{G}' \mathbf{A} \quad (6)$$

Here, a_D and a_A normalize the wave functions for the initial and final states and correct the donor/acceptor energies for donor-bridge and acceptor-bridge interactions.^{43,44} \mathbf{D} and \mathbf{A} represent the interactions between the donor (acceptor) and the bridge diabatic states. \mathbf{G}' is the effective Green's function for the bridge. (Note that the pure bridge Green's function has an additional overlap term⁴⁵ that cancels with terms in the donor (acceptor)-bridge interactions.)

$$D_\mu = (E\mathbf{S} - \mathbf{H})_{D\mu} \quad (7)$$

$$A_\nu = (E\mathbf{S} - \mathbf{H})_{\nu A} \quad (8)$$

$$G'_{\mu\nu} = (E\mathbf{S}^B - \mathbf{H}^B)^{-1}_{\mu\nu} \quad (9)$$

\mathbf{S} is the overlap matrix and \mathbf{H} is the electronic Hamiltonian matrix. \mathbf{S}^B and \mathbf{H}^B are matrices for the bridge subsystem. E is the tunneling energy. If E is close in energy to the frontier orbitals of the bridge, then hopping transport may compete with the superexchange (tunneling) transport mechanism.⁴⁶

The *Pathways* model is predictive and has been used both to interpret¹⁹ and to design protein ET systems.²³ Previous studies have compared *Pathways* and explicit quantum predictions for T_{DA} .²⁷ The *Pathways* metric PA_j is associated with wave function tail amplitudes and can be compared with other coupling metrics and score functions.^{24,25,27–29,31–36} We examine time-averaged magnitudes of atomic orbital coefficients to define a conformationally averaged electronic propagation score function that is a multiorbital analogue of *Pathways*-based metrics. The score functions describe the relative coupling strength at specific protein surface sites. The time-averaged quantum

chemical scoring function “QC” is computed at the extended-Hückel level for the protein and the surrounding water. We describe how the conformational averaging over ET bridge geometries influences the donor–acceptor interaction. Comparison among the score functions suggests acceptable approximation levels for describing electronic propagation through proteins.

2. Computational Methods

Electronic Propagation. The localized donor and acceptor molecular orbitals are ϕ_D and ϕ_A , and the protein atomic orbitals are ϕ_ν . The initial and final ET states are

$$\psi^{(i)}(E) = a_D(E)\phi_D + \sum_\nu C_\nu^{(i)}(E)\phi_\nu \quad (10)$$

$$\psi^{(f)}(E) = a_A(E)\phi_A + \sum_\nu C_\nu^{(f)}(E)\phi_\nu \quad (11)$$

These are quasi-degenerate with electron-tunneling energy E .¹⁹ The coefficients of the atomic orbitals in eqs 10 and 11 are⁴³

$$C_\nu^{(i)}(E) = -a_D(E) \sum_\mu D_\mu^\dagger(E) G'_{\nu\mu}(E) \quad (12)$$

$$C_\nu^{(f)}(E) = -a_A(E) \sum_\mu G'_{\nu\mu}(E) A_\mu(E) \quad (13)$$

and

$$a_D(E) = 1/\sqrt{1 + 2 \sum_\mu C_\mu^{(i)}(E) S_{D\mu} + \sum_{\mu\nu} C_\mu^{(i)}(E) S_{\mu\nu} C_\nu^{(i)}(E)} \quad (14)$$

$$a_A(E) = 1/\sqrt{1 + 2 \sum_\mu C_\mu^{(f)}(E) S_{D\mu} + \sum_{\mu\nu} C_\mu^{(f)}(E) S_{\mu\nu} C_\nu^{(f)}(E)} \quad (15)$$

The $C_\nu(E)$ coefficients indicate how the localized state wave functions propagate through the protein and solvent. We use these coefficients (and associated averages) to define a score function. In the specific calculations here, we use an extended-Hückel Hamiltonian to compute wave function amplitudes in eqs 10–15.

Substituting eq 12 into eq 6, T_{DA} is

$$T_{DA}(E) = -a_A(E) \mathbf{C}^{(i)}(E) \mathbf{A}(E) \quad (16)$$

where $\mathbf{C}^{(i)}(E)$ is a vector with components $C_\nu^{(i)}(E)$. The dominant components of $\mathbf{A}(E)$ are localized near the acceptor. Substituting eq 5 into eq 3, the *Pathways* T_{DA} value is

$$T_{DA} = (b/b_D) PA_j \epsilon_{j,j+1}^X(r_{j,j+1}) \quad (17)$$

where $j + 1$ is the index of a site next to atom j where the acceptor could be located. b (units of energy) and b_D (unitless) appear in eqs 3 and 5. Equation 16 indicates that the electronic coupling arises from products of atomic orbital coefficients of the donor-localized wave function of the protein $\mathbf{C}^{(i)}(E)$ and the acceptor interaction with bridge atomic orbitals $\mathbf{A}(E)$. A measure of the magnitude of electronic amplitude on the bridge orbitals k is

$$QC_k(E) \equiv \sqrt{C_k^{(i)}(E) S_{kk} C_k^{(i)\dagger}(E)} \quad (18)$$

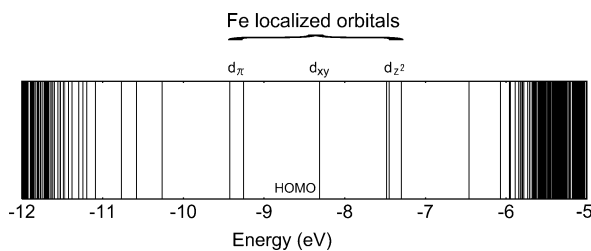


Figure 1. Molecular orbital energies of the heme and its ligand near the HOMO–LUMO gap, computed at the extended-Hückel level.

$C_k^{(i)}(E)$ contains the atomic orbital coefficients of atoms in group k

$$C_k^{(i)}(E) \equiv \begin{pmatrix} C_{\xi}^{(i)}(E) \\ C_{\xi+1}^{(i)}(E) \\ \vdots \end{pmatrix} \quad (19)$$

where $\xi, \xi + 1, \dots$ are atomic orbital indices for atoms in group k . S_{kk} is the overlap matrix for atoms in group k

$$S_{kk} \equiv \begin{pmatrix} S_{\xi, \xi} & S_{\xi, \xi+1} & \cdots \\ S_{\xi+1, \xi} & S_{\xi+1, \xi+1} & \cdots \\ \vdots & \vdots & \ddots \end{pmatrix} \quad \xi, \xi + 1, \dots \in k \quad (20)$$

For group j of an atom, S_{jj} is a unit matrix and QC_j is

$$QC_j = \sqrt{\sum_{\xi=s, p, x, \dots} |C_{\xi}^{(i)}(E)|^2} \quad (21)$$

When eqs 16 and 17 are compared, the physical interpretation of $C_j^{(i)}(E)$ is analogous to the PA_j term.¹⁹ At the donor, $QC_D = a_D(E)$ and $PA_D = b_D$. The $a_D(E)$ value indicates how much the donor orbital contributes to the initial state for the electron tunneling with tunneling energy E . The $a_D(E)$ factor corrects T_{DA} in eq 6 based on the mixing of the donor and bridge in the wave functions (eq 10).^{43,44}

Molecular Dynamics Simulation. We used sperm whale myoglobin (PDB code 104M)^{47,48} as a test structure. The mole-

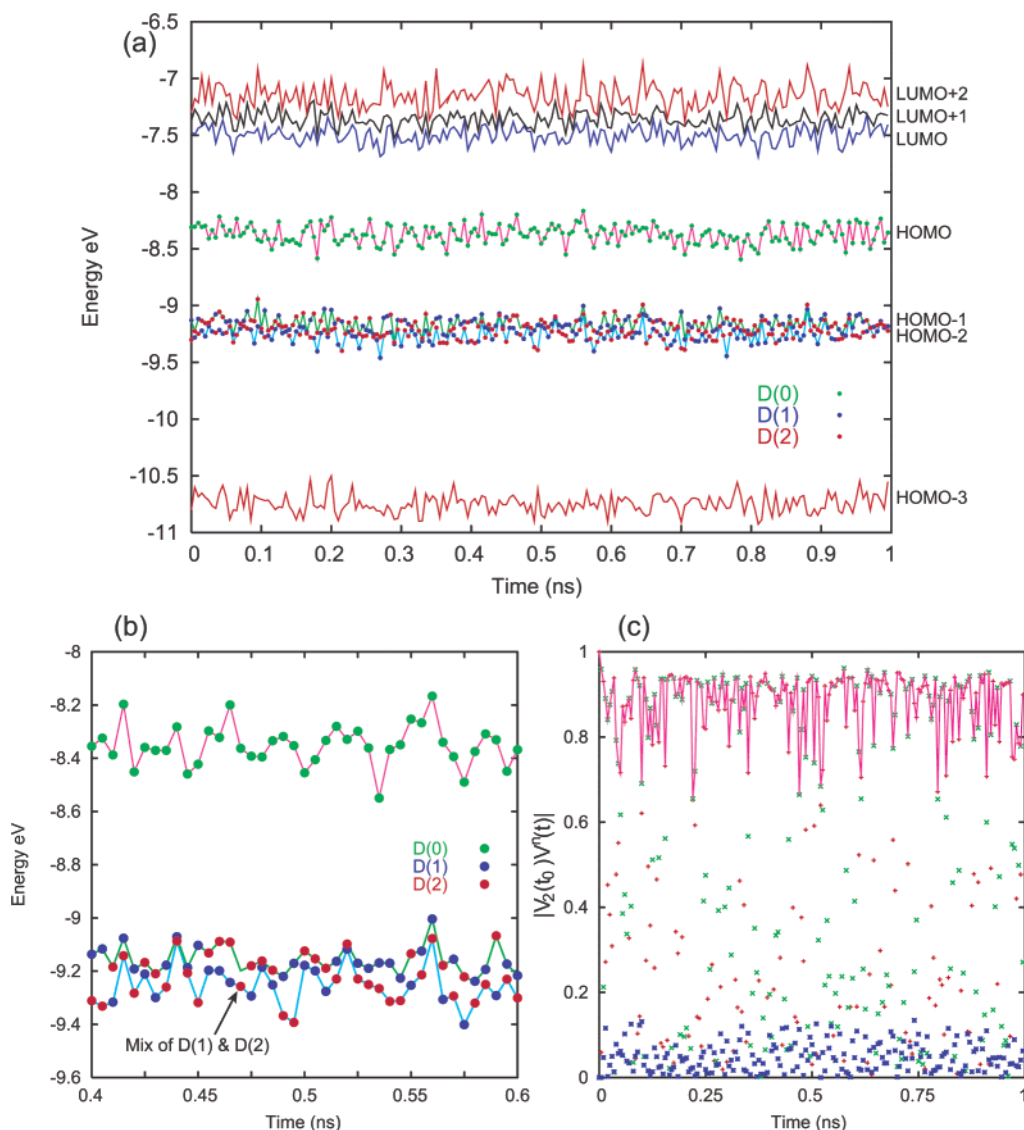


Figure 2. (a) Time-dependent extended-Hückel orbital energies of heme plus ligand. Lines are energy eigenvalues of the HOMO–3 (red), HOMO–2 (cyan), HOMO–1 (green), HOMO (purple), LUMO (blue), LUMO+1 (black), and LUMO+2 (red) ordered from the bottom. The horizontal axis is the time (ns). Green, red, and blue spots indicate donor types $D(0)$, $D(1)$, and $D(2)$, respectively. (b) Time-dependent extended-Hückel energy of heme plus ligands focused around HOMO, HOMO–1, and HOMO–2. Notation is the same as in part a. (c) $|V_2(t_0)V^n(t)|$ used in the $D(2)$ search. The red +, green x, and blue * indicate HOMO–2, HOMO–1, and HOMO, respectively. The purple line indicates the chosen $D(2)$. t_0 of the first snapshot is used.

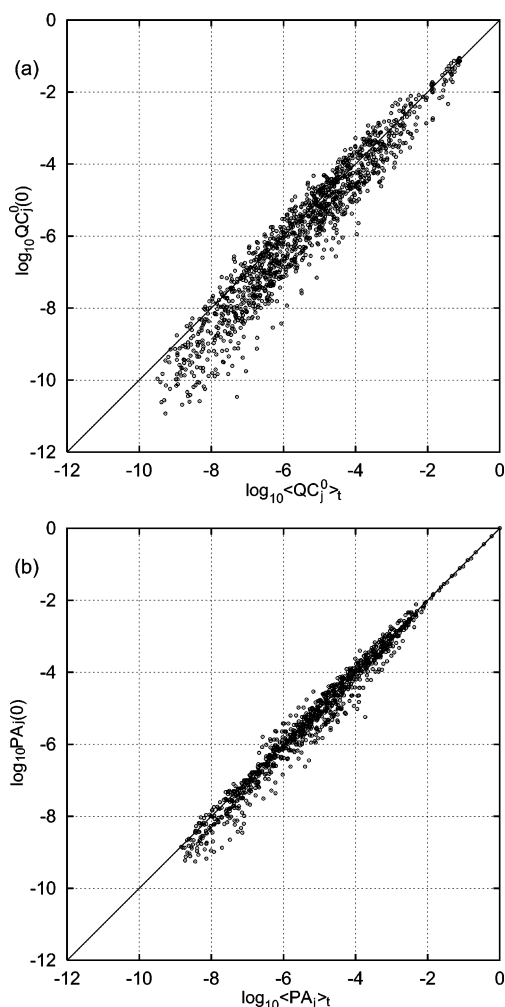


Figure 3. Comparison of (a) $QC_j^0(t_1)$, (b) $PC_j(t_1)$, and the corresponding average values for 200 MD snapshots. $E = -8.4$ eV for QC calculations. Axes are the log of QC/PC.

cule was equilibrated in a box with 4010 TIP3 water molecules, 4 sodium ions, and 4 chloride ions (0.05 M ionic strength) using NAMD2.⁴⁹ All Lys and Arg residues were protonated, and all Asp and Glu residues were deprotonated because they are located on the protein surface. A box size of approximately $60 \times 48 \times 48 \text{ \AA}^3$ was employed using the flexible box size option. The simulation was run with periodic boundary conditions and a Langevin thermostat. The temperature was set to 310 K. The 2 ns simulations were performed, and 200 snapshots were taken every 5 ps during the last 1 ns of the simulation.

Quantum and Pathways Analysis. The extended-Hückel Hamiltonian uses

$$H_{\mu\nu} = \begin{cases} \alpha_\mu & (\mu = \nu) \\ 1.75S_{\mu\nu}(\alpha_\mu + \alpha_\nu)/2 & (\mu \neq \nu) \end{cases} \quad (22)$$

$S_{\mu\nu}$ was computed using ICON8⁵⁰ with a Slater-type orbital basis set. Extended-Hückel and orbital parameters were taken from a density functional study.⁵¹ ITPACK2C⁵² was used to solve the linear equations for $C^{(i)}$. The EIGRS subroutine is used to diagonalize the Hamiltonian.⁵³ HARLEM was used to compute PA_j values.⁵⁴ We used the same values of a_D (computed) and b_D in the QC_j and PA_j calculations.

Donor Orbitals. In full protein calculations at the extended-Hückel level, we found an energy gap for the protein between -11 and -6 eV (Figure 1). HOMO-1 and HOMO-2 orbitals are derived from the three approximately octahedral field t_{2g}

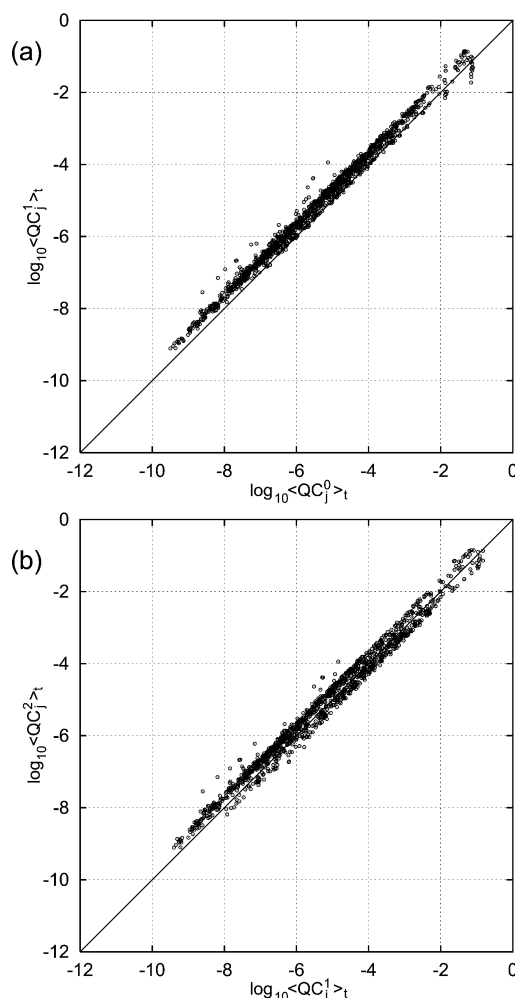


Figure 4. Comparison between (a) QC_j^0 and QC_j^1 , and (b) QC_j^1 and QC_j^2 . $E = -8.4$ eV. Axes are the log of QC.

orbitals of the heme iron, where HOMO is the highest occupied molecular orbital and HOMO- m is the m th molecular orbital below the HOMO. The HOMO is derived from the iron d_{xy} orbital that mixes with heme π -cloud.^{55,56} The HOMO localizes more than 90% (based on Mulliken population analysis) on the iron. The HOMO-1 and HOMO-2 are localized more than 50% on the iron atom. We chose these three molecular orbitals as the donor states. The d_{z^2} Fe orbital dominates the LUMO+1 (Figure 1), where the LUMO is the lowest occupied molecular orbital and the LUMO+ m is the m th molecular orbital above the LUMO. The d_{z^2} orbital appears in Figure 1 because we did not attach a sixth ligand to the heme. The d_{z^2} orbital is expected to be located much higher in energy than is shown in Figure 1 when the heme has a bound sixth ligand (for example, about -3 eV when the heme has two histidine ligands).

In the coupling calculations, we further simplified the donor orbital ϕ_D description. We approximate it as a linear combination of Fe atomic orbitals, because the donor state is dominantly metal-localized. We computed the extended-Hückel orbitals for the heme and its histidine ligand, replacing the C_α of the histidine with a hydrogen atom. Finally, we truncated the computed molecular orbitals to a single-donor atomic orbital on the iron. Coefficients of atomic orbitals in ϕ_D are given from each Fe-localized molecular orbital.

The eigenvalues of the isolated heme with its ligand (five-coordinate Fe) are shown in Figures 2a and 2b for molecular dynamics (MD) snapshot geometries. The lines indicate

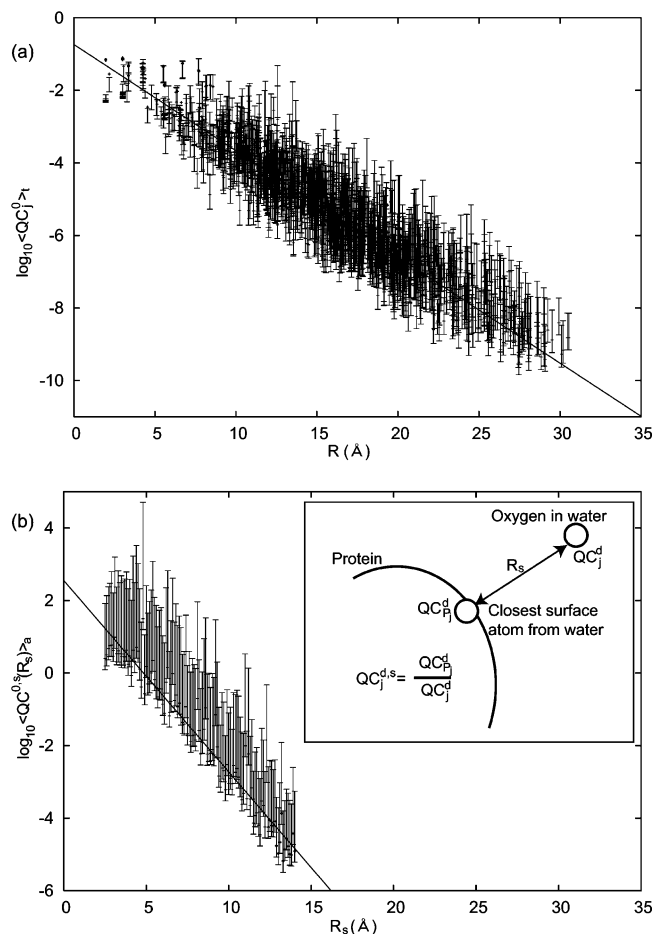


Figure 5. Distance dependence of $\langle QC_j^0 \rangle_t$ with $E = -8.4$ eV. Each point has error bars. (a) The horizontal axis is the distance from the donor to specific atoms in the protein. The vertical axis is the log of $\langle QC_j^0 \rangle_t$ at specific atoms. The slope of the fitted line (solid) is 0.67 Å^{-1} . (b) The horizontal axis is the distance from the protein surface to water oxygen atoms. The vertical axis is the log of $\langle QC_j^0(R_s) \rangle_a$ at R_s distances (see box). The slope of the fitting line (solid line) is 1.2 Å^{-1} .

LUMO+2 through HOMO-3. The HOMO-1 and HOMO-2 (and also LUMO to LUMO+2) switch their energy ordering between snapshots. We defined time-dependent donor orbitals $D(d)$ ($d = 0, 1$, and 2). The donor HOMO, HOMO-1, and HOMO-2 in the first snapshot ($t_0 = 0$ ps) are labeled $D_0(0)$, $D_0(1)$, and $D_0(2)$, respectively. The normalized eigenvector of the electronic Hamiltonian of the heme plus ligand is $\mathbf{V}_d(t_0)$ (d is the donor index). We assume that the donor orbital $D_k(d)$ at time t_k retains approximately the same eigenvector $\mathbf{V}_d(t_0)$ as at time t_0 . t_k is the time of the k th snapshot. We computed eigenvectors $\mathbf{V}^n(t_k)$ for energies between the frontier orbitals of the protein (without the cofactor) for each snapshot ($n = \text{HOMO}, \text{HOMO} \pm 1, \text{HOMO} \pm 2, \dots$ for the full system) and chose the eigenvector $\mathbf{V}_d(t_k)$ of the donor $D_k(d)$ from $\mathbf{V}^n(t_k)$ with $|\mathbf{V}_d(t_0) \mathbf{V}^n(t_k)|$ closest to 1. We searched the range of energy eigenvalues from -11 to -8 eV for orbitals n . $|\mathbf{V}_0(t_0) \mathbf{V}^n(t_k)|$ is plotted at time $t_0 = 0$ ps in Figure 2c. The plot shows how to distinguish $D(2)$ from $D(0)$ and $D(1)$ among the HOMO, HOMO-1, and HOMO-2. $D(0)$ and $D(1)$ are also distinguished by the same method. If the sign of $\mathbf{V}_d(t_0) \mathbf{V}_n(t_k)$ is negative, then we used $-\mathbf{V}_n(t_k)$ instead of $\mathbf{V}_n(t_k)$ to avoid the sign change between $\mathbf{V}_d(t_0)$ and $\mathbf{V}_d(t_k)$. The eigenvalues of $\mathbf{V}_d(t_k)$ ($d = 0, 1$, and 2) are plotted in Figure 2a. We found two cases of degeneracy among 200 snapshots for $D(1)$ and $D(2)$. At those

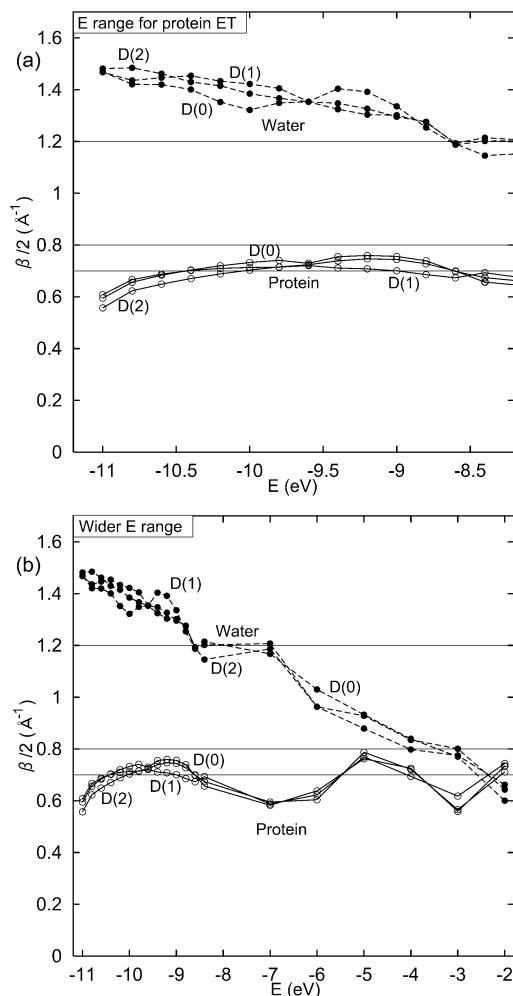


Figure 6. Energy dependence of the distance decay factor $\beta/2$ for log $\langle QC_j^d \rangle_t$. Results for donor types $D(0)$, $D(1)$, and $D(2)$ are shown. (a) Energy range for ET in protein and (b) a wider energy range. The vertical axis is $\beta/2$ calculated for $\langle QC_j^d \rangle_t$. The open circles indicate $\beta/2$ protein values. The solid circles indicate $\beta/2$ through water from the protein interface. The line at $\beta/2 = 0.7$ indicates the experimental value for helical proteins.²³ The line at $\beta/2 = 0.8$ indicates the experimental value for glassy water¹⁶ and ab initio calculation of water ET.^{27,18} The line at $\beta/2 = 1.2$ indicates the water as estimated by Larsson.¹⁵

specific times, any of the $D(1)$ and $D(2)$ linear combinations can be chosen (e.g., 470 ps, Figure 2b).

T_{DA} is computed using linear combinations of $C_{\nu}^{(i)}$ over the three donor orbitals. The contribution from each donor orbital is determined by the symmetry of the donor orbital, the tunneling energy, and the acceptor orbital. We show only single-donor orbital results for simplicity.

Tunneling Energy. For tunneling energies close to the protein HOMO, the electronic coupling is dominated by hole mediation through occupied orbitals of the bridge. For tunneling energies near the protein LUMO, the electronic coupling is dominated by electron mediation through unoccupied bridge orbitals. ET through proteins is typically dominated by hole transfer in the bridge.⁵⁷ The transition state energy as the tunneling energy for a heme protein (cytochrome *c*) was estimated at 0.67 eV above the heme-localized HOMO with a tunneling energy of -10.68 eV by Siddarth and Marcus.⁴¹ Here, the tunneling energy is approximately -10 eV. T_{DA} changes little with the tunneling energy over the HOMO-LUMO gap in our analysis. So, this specific energy is not important. The

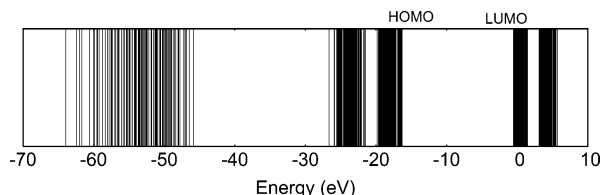


Figure 7. Molecular orbital energies of a water cluster including 88 water molecules, computed at the extended-Hückel level.

choice may become important for ET through water, as discussed in the next section.

The two-state approximation fails as E approaches bridge resonances. We examine the tunneling energy dependence of the initial state in Appendix A.

The tunneling energy depends on the electronic structure of the protein, and predictions of this dependence depend on the method. We show the comparison of the HOMO and LUMO energies at the extended-Hückel level and the Hartree–Fock (HF) level in Appendix B.

3. QC Score Function

Sensitivity of QC to Thermal Fluctuations. We explored the sensitivity of the QC score functions to conformational fluctuations using 200 MD snapshots taken every 5 ps. A root-mean-square QC_j , equal to the square root of the averaged Mulliken population at site j is

$$\langle QC_j^d \rangle_t = \sqrt{\frac{1}{N} \sum_{k=1}^N (QC_j^d(t_k))^2} \quad (23)$$

$QC_j^d(t_k)$ is the value of QC at j for MD time step t_k using the donor orbital $D(d)$ ($d = 0, 1$, and 2). N is the number of snapshots. Figure 3a shows the fluctuations of $QC_j^0(t_k)$ along the trajectory. At many geometries, $QC_j^0(0)$ is much smaller than $\langle QC_j^0 \rangle_t$, because of destructive quantum interference.^{1–8} Pathways analysis contains no explicit multipath interferences, but structural fluctuations can change the dominant pathways and their couplings. The conformationally averaged PA value is

$$\langle PA_j \rangle_t = \sqrt{\frac{1}{N} \sum_{k=1}^N (PA_j(t_k))^2} \quad (24)$$

We find that PA_j values fluctuate less than QC_j^0 values (Figure 3b).

Comparison between Donors. Figures 4a and 4b compare the score function $\langle QC_j^0 \rangle_t$ with $\langle QC_j^1 \rangle_t$ and $\langle QC_j^1 \rangle_t$ with $\langle QC_j^2 \rangle_t$ for donor orbitals. Although QC_j^d depends on the donor type, $D(0)$, $D(1)$, and $D(2)$ couplings are strongly correlated. We show $D(0)$ with $E = -8.4$ eV (energy close to the $D(0)$ orbital and near the center of the protein HOMO–LUMO gap) in most of this paper.

Distance Decay of the Score Functions. We calculated the average distance decay parameter $\beta/2$ for the score function. Figure 5a shows $\log \langle QC_j^0 \rangle_t$ versus distance from the donor. The plot indicates a rough linear correlation between distance and $\log \langle QC_j^0 \rangle_t$, as expected.^{13–18} The score function decays with $\beta/2 = 0.67 \text{ \AA}^{-1}$, in agreement with experimental rate decays ($\beta/2 = 0.7 \text{ \AA}^{-1}$) in helical proteins.^{23,58,59} The $\langle QC_j^0 \rangle_t$ -based $\beta/2$ value depends weakly on the tunneling energy. We find $\beta/2 = 0.56\text{--}0.76 \text{ \AA}^{-1}$ for tunneling energies between -11.0 eV and -8.4 eV (Figure 6a).

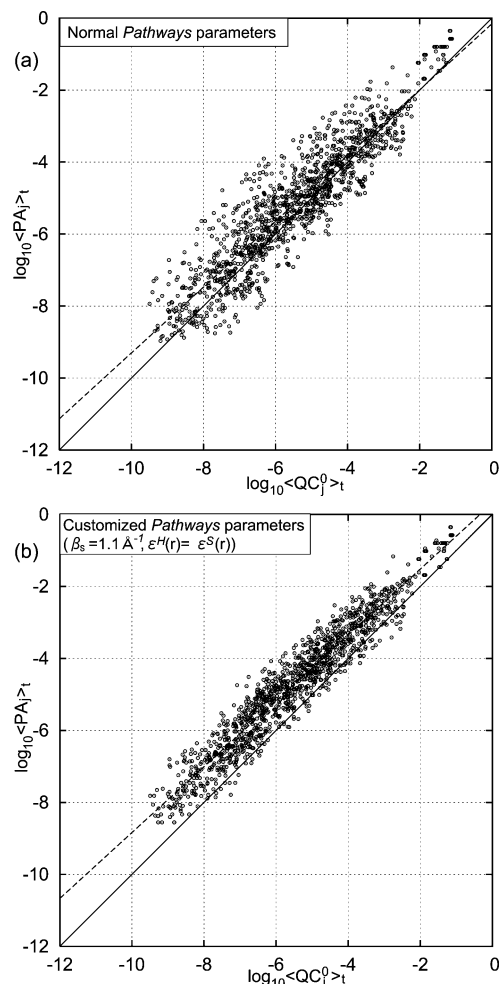


Figure 8. Comparison of $\langle QC_j^0 \rangle_t$ with $\langle PC_j \rangle_t$ for the protein (a) with low-penalty hydrogen-bond and high-penalty through-space parameters (normal Pathways) for $\langle PC_j \rangle_t$ and (b) high-penalty hydrogen-bond and low-penalty through-space parameters ($\beta_s = 1.1 \text{ \AA}^{-1}$, $\epsilon^H(r) = \epsilon^S(r)$) for $\langle PC_j \rangle_t$. Parameter values $b_D = 7.4$ and $E = -8.4$ eV are chosen. The horizontal axis is the log of $\langle QC_j^0 \rangle_t$ in the protein. The vertical axis is the log of $\langle PC_j \rangle_t$ corresponding to $\langle QC_j^0 \rangle_t$. The solid line with unit slope corresponds to perfect correlation between $\langle QC_j^0 \rangle_t$ and $\langle PC_j \rangle_t$ values. The dashed lines have slopes of 0.91.

QC in Water. QC analyzes coupling strength from the donor into water surrounding the protein. Because water is mobile and its structure strongly influences QC_j , we define an averaged solvent score function for distances R_s from the protein surface

$$\langle QC^{d,s}(R_s) \rangle_a = \sqrt{\frac{1}{\sum_{l=1}^N N_l(R_s)} \sum_{k=1}^N \sum_{j=1}^{N_k(R_s)} (QC_j^d(t_k))^2} \quad (25)$$

where

$$(QC_j^{d,s}(t_k))^2 = \frac{QC_j^d(t_k)^2}{QC_{P_j}^d(t_k)^2} \quad (26)$$

j indexes oxygen atoms of the water. P_j is the closest heavy atom to atom j on the protein surface. R_s is the distance between atoms j and P_j . $N_k(R_s)$ is the number of water oxygen atoms at distance R_s at time t_k . We exclude data for distances less than 2.5 \AA because of the small sample size and the difficulty of

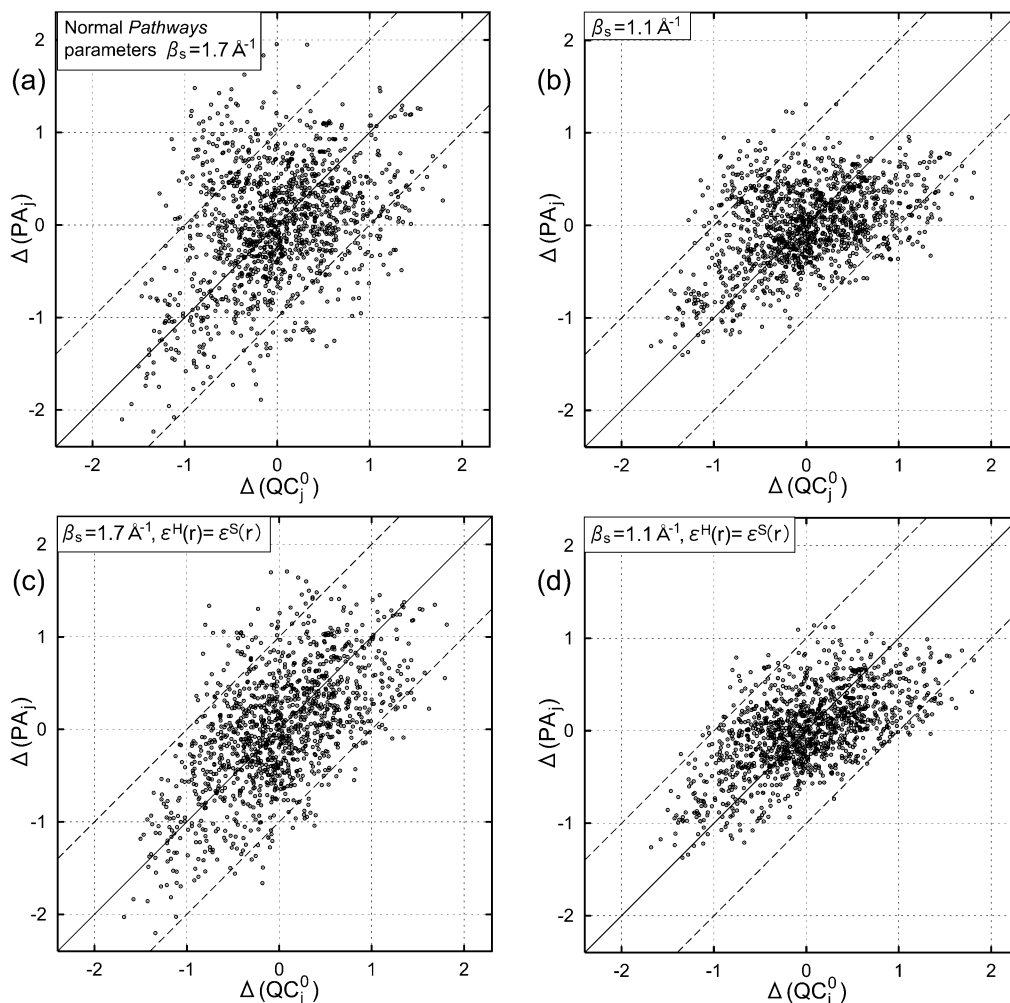


Figure 9. Comparison of $\Delta(QC_j^0)$ with $\Delta(PA_j)$ in the protein (a) with typical parameters for *Pathways* analysis, (b) low-penalty through-space parameters for $\langle PC_j \rangle$, (c) high-penalty hydrogen-bond parameters for $\langle PC_j \rangle$, and (d) low-penalty through-space and high-penalty hydrogen-bond parameters for $\langle PC_j \rangle$; $E = -8.4$ eV is used. Parameters for $\langle PA_j \rangle$ (eq 27) are (a) $\beta/2 = 0.66 \text{ \AA}^{-1}$, (b) $\beta/2 = 0.62 \text{ \AA}^{-1}$, (c) $\beta/2 = 0.79 \text{ \AA}^{-1}$, and (d) $\beta/2 = 0.66 \text{ \AA}^{-1}$. The horizontal axis is $\Delta(QC_j^0)$. The vertical axis is $\Delta(PA_j)$ at corresponding atoms to $\Delta(QC_j^0)$. $\Delta(QC_j^0)$ is equal to $\Delta(PA_j)$ on the solid line. The broken lines indicate a 10-fold difference between $\Delta(QC_j^0)$ and $\Delta(PA_j)$.

defining a reference protein surface. Figure 5b shows $\beta/2 \approx 1.21 \text{ \AA}^{-1}$, close to Larsson's earlier estimate of the electronic coupling decay through water ($\beta/2 = 1.2 \text{ \AA}^{-1}$),¹⁵ but larger than recent results from experiments ($\beta/2 = 0.8 \text{ \AA}^{-1}$)¹⁶ and ab initio ($\beta/2 = 0.7\text{--}0.9 \text{ \AA}^{-1}$)^{17,18} or INDO calculations ($\beta/2 = 1.0 \text{ \AA}^{-1}$).¹⁷

Figure 6 shows the distance decay factors computed for the water as a function of the tunneling energy. Although $\beta/2$ for protein-mediated ET does not depend strongly on E , $\beta/2$ through water does depend strongly on E . The decay factors for water are $\beta/2 \approx 1.15\text{--}1.48 \text{ \AA}^{-1}$ for tunneling energies between -11.0 and -8.4 eV (Figure 6a). Figure 7 shows the extended-Hückel level energy eigenvalues of an 88 molecule water cluster chosen from an equilibrated MD simulation. The HOMO–LUMO gap is between -16.3 and -0.6 eV, much larger than the energy gap in proteins (Figure 1). We computed $\beta/2$ using tunneling energies placed near the antibonding orbitals of the protein (Figure 1) and near the water LUMO (Figure 7). Using tunneling energies near the water LUMO, we obtained smaller values of $\beta/2$ than in the protein energy gap, and these water values agree with glassy water experiments ($\beta/2 = 0.8 \text{ s}^{-1}$)¹⁶ and ab initio calculations ($\beta/2 = 0.7\text{--}0.9 \text{ s}^{-1}$)^{17,18} (Figure 6b). The $\beta/2$ factor for water is large at energies below the protein LUMO and small at energies above the protein LUMO (Figure 6b).

The water HOMO is strongly localized on the oxygen atom and independent of the molecular geometry because the $1B_1$ orbital is dominated by the oxygen lone pair.⁶⁰ The overlap between HOMOs of different water molecules is small, and these interactions are weak. This may be the reason that the $\beta/2$ values for water are so large for the hole transfer through water. The water LUMO has contributions from both the oxygen and the hydrogen atomic orbitals and is less localized than the water HOMO. At higher tunneling energies, the electronic coupling is dominated by electron rather than hole superexchange, and $\beta/2$ becomes small (close to ab initio¹⁸ and experimental results¹⁶). We expect that water-mediated ET can be accelerated when coupling through water empty orbitals becomes significant. However, because of the energetics at the extended-Hückel level such acceleration is not apparent. The reason that the extended-Hückel level prediction is different from experiments and ab initio calculations likely arises from the extended-Hückel parameters and minimum basis set. In the following sections, we focus on ET through the protein.

4. Score Function Results

QC versus PA. Figure 8 shows that the distance decay of $\langle QC_j^0 \rangle$ is similar to that of $\langle PA_j \rangle$. Because $\langle QC_j^d \rangle$ values ($d =$

TABLE 1: Correlations between $\Delta(QC_j^0)$ and $\Delta(PC_j)$ with Customized *Pathways* Parameters

PC parameter	correlation coefficient			fitted slope		
	$D(0)$	$D(1)$	$D(2)$	$D(0)$	$D(1)$	$D(2)$
$\beta_s = 1.7$ (\AA^{-1})	0.35	0.27	0.28	0.37	0.28	0.30
$\beta_s = 1.1$	0.44	0.31	0.35	0.31	0.22	0.25
$\beta_s = 0.9$	0.47	0.33	0.38	0.27	0.19	0.22
$\beta_s = 1.7/\epsilon^H(r) = \epsilon^S(r)$	0.60	0.47	0.51	0.64	0.49	0.55
$\beta_s = 1.1/\epsilon^H(r) = \epsilon^S(r)$	0.61	0.46	0.52	0.43	0.32	0.36
$\beta_s = 0.9/\epsilon^H(r) = \epsilon^S(r)$	0.60	0.44	0.50	0.34	0.24	0.28

0, 1, and 2) are similar, we compare only the $\langle QC_j^0 \rangle_t$ and $\langle PA_j \rangle_t$ results. We used $b_D = 0.74 \approx a_D$ for the $\langle PA_j \rangle_t$ to fit the value of $\langle PA_D \rangle_t$ to $\langle QC_D^0 \rangle_t$ (the score function for the donor). There are strong correlations (0.92 correlation coefficient, 0.91 slope) between these two score functions in myoglobin because both values have roughly exponential distance decay. $\langle QC_j^0 \rangle_t$ and $\langle PA_j \rangle_t$ give similar average decay factors ($\beta/2 = 0.67$ and 0.66 \AA^{-1} , respectively).

We also calculated the analogues of previously defined measures of coupling “hot” and “cold” spots^{24,25}

$$\Delta(PA_j) = \log_{10} \left(\frac{\langle PA_j \rangle_t}{\exp[-\beta(R_j - R_0)/2]} \right) \quad (27)$$

and

$$\Delta(QC_j^0) = \log_{10} \left(\frac{\langle QC_j^0 \rangle_t}{\exp[-\beta(R_j - R_0)/2]} \right) \quad (28)$$

where β and R_0 are fitting parameters. R_j is the distance between the donor and atom j . These functions slow the influence of the protein fold on the electronic coupling. Figure 9a shows the correlations between $\Delta(QC_j^0)$ ($\beta/2 = 0.67 \text{ \AA}^{-1}$) and $\Delta(PA_j)$ ($\beta/2 = 0.66 \text{ \AA}^{-1}$). We also calculated $\langle PA_j \rangle_t$ using *Pathways* parameters with softer through-space decay factors. The top-right (bottom-left) quadrants in Figure 9 show values of $\langle PA_j \rangle_t$ and of $\langle QC_j^0 \rangle_t$ that are larger (smaller) than the exponential functions. Points in these two quadrants have a strong correlation between $\Delta(PA_j)$ and $\Delta(QC_j^0)$ values. The two other quadrants have smaller (larger) $\Delta(PA_j)$ than $\Delta(QC_j^0)$ values. Points in the bottom-right and top-left quadrants have a disparity between $\langle PA_j \rangle_t$ and $\langle QC_j^0 \rangle_t$ values. Computed correlation coefficients between $\Delta(QC_j^0)$ and $\Delta(PA_j)$ are 0.35, 0.44, 0.60, and 0.61 for Figures 9a, 9b, 9c, and 9d, respectively. Figure 9d shows a stronger correlation between methods than Figure 9a. Table 1 shows the correlation coefficients between $\Delta(QC_j^0)$ and $\Delta(PA_j)$ and the linear fitting slope with different parameters and donor types. $\beta_s = 1.1 \text{ \AA}^{-1}$ ($\epsilon^H(r) = \epsilon^S(r)$) produces the strongest correlation between $\Delta(QC_j^0)$ and $\Delta(PA_j)$ values. These correlation coefficients depend somewhat on donor type. However, the qualitative dependence on *Pathways* parameters is similar for different donors. Figures 10a and 10b show the myoglobin structure and the regions with significant differences in correlation coefficients. The F α -helix directly couples to the heme through the histidine ligand, and *Pathways* analysis indicates that the strongest pathways in this helix include the α -helix hydrogen bonds. In this region of the protein, $\Delta(QC_j^0)$ is as much as 100 times smaller than $\Delta(PA_j)$. The A α -helix at the bottom of Figure 10a has $\Delta(QC_j^0)$ much larger than $\Delta(PA_j)$. The A-helix axis is perpendicular to the line joining the heme edge and the helix center. Through-space and through-residue pathways dominate the coupling. $\Delta(QC_j^0)$ is as much as 10

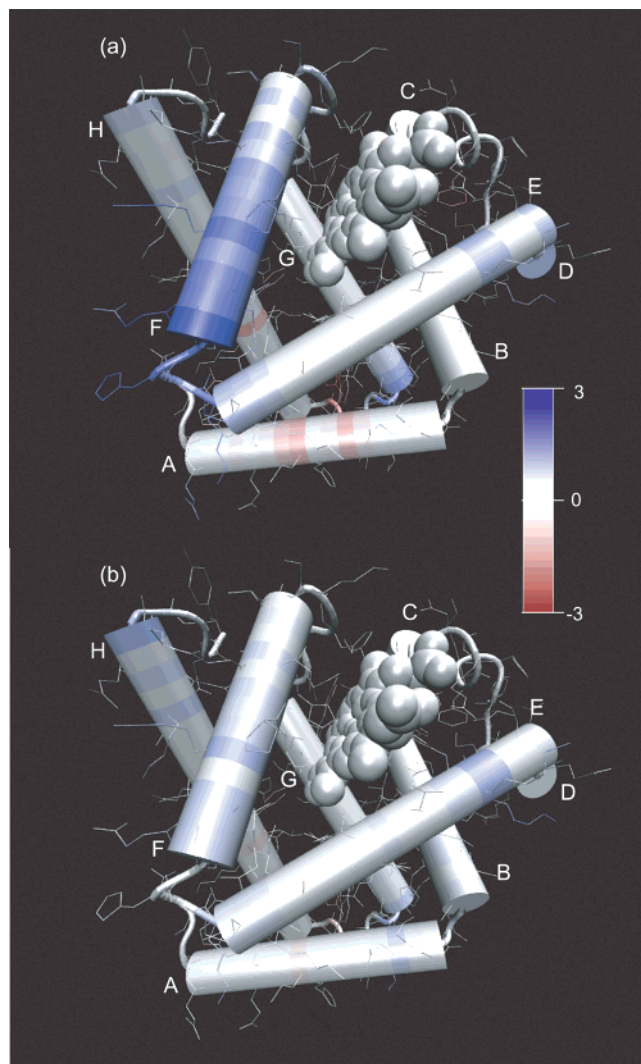


Figure 10. Difference between hot and cold spot maps ($\Delta(PC_j) - \Delta(QC_j^0)$) for myoglobin (a) with typical *Pathways* analysis parameters and (b) high-penalty hydrogen-bond and low-penalty through-space parameters ($\beta_s = 1.1 \text{ \AA}^{-1}$, $\epsilon^H(r) = \epsilon^S(r)$) for $\langle PC_j \rangle_t$. The blue color indicates atoms for $\Delta(QC_j^0) \ll \Delta(PC_j)$, and the red color indicates $\Delta(QC_j^0) \gg \Delta(PC_j)$. Letters are indices for helices. The figures are rendered with VMD⁶²

times larger than $\Delta(PA_j)$ in this case. Figure 10b shows that differences between $\Delta(QC_j^0)$ and $\Delta(PA_j)$ values arise largely from the hydrogen-bond and through-space parametrizations. The weakest correlation in Figure 10a vanishes in Figure 10b when the hydrogen-bond decay factors decrease and the through-space decay factors increase. $\langle QC_j^0 \rangle_t$ at the extended-Hückel level describes the hydrogen bonds differently from the *Pathways* model.²⁷ Figure 8b compares $\langle QC_j^0 \rangle_t$ with $\langle PA_j \rangle_t$ for $\beta_s = 1.1 \text{ \AA}^{-1}$ and $\epsilon^H(r) = \epsilon^S(r)$. The scatter in Figure 8b (high-penalty hydrogen-bond and low-penalty through-space decay factors) is less than in Figure 8a (low-penalty hydrogen-bond and high-penalty through-space decay factors).

5. Discussion

We have described a thermally averaged electronic propagation score function for proteins and solvent. The score function has an average distance decay consistent with experimental values for helical proteins.^{23,58,59} We compared the *Pathways* and quantum chemical score functions for myoglobin and found qualitative agreement, especially if *Pathways* parameters are

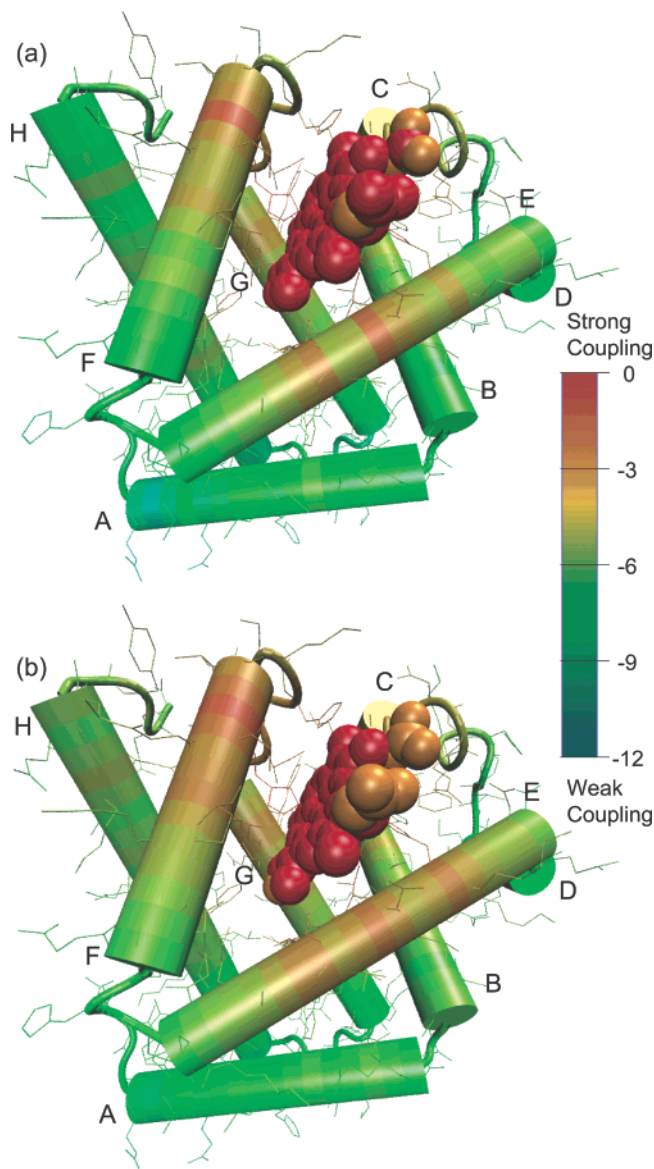


Figure 11. Electronic coupling map from the heme iron in myoglobin (a) $\langle QC_j^0 \rangle_t$ and (b) $\langle PC_j \rangle_t$ ($\beta_s = 1.1 \text{ \AA}^{-1}$, $\epsilon^H(r) = \epsilon^S(r)$). The color indicates the strength of the electronic coupling (red \gg blue). The color scale is logarithmic.

tuned so that $\epsilon^H(r) = \epsilon^S(r)$ and $\beta_s = 1.1 \text{ \AA}^{-1}$. Figure 11 shows the distribution of the electronic couplings computed with these two approaches. Both maps produce similar qualitative average coupling decays with distance.

The activation limited bimolecular ET rate is determined by the average^{37,38}

$$k_r = \sum_i K_a^i k_{ET}^i \quad (29)$$

K_a^i is a binding constant for geometry i . Geometries with large k_{ET}^i (roughly proportional to the square QC or PA) can control k_r , even if they are minority species.³⁷ That is, the red or orange surface regions can control bimolecular ET rates. Equations 16 and 17 link QC and PA to the electronic couplings. These dynamically averaged score functions are therefore useful to estimate the local electronic couplings to the protein surface. The maps in Figure 11 help to locate viable functional docking positions for interprotein ET and more beyond earlier views of the individual proteins.^{36–39}

The QC_j^0 values for specific snapshots may produce much smaller couplings than the average, $\langle QC_j^0 \rangle_t$ (Figure 3a), because of destructive interference. Time-averaged couplings, therefore, can be very different in magnitude from the couplings in specific “snapshot” geometries. As such, time averaging smooths out dramatic pathway interference effects. For protein-mediated electronic coupling, PA_j correlates with $\langle PA_j \rangle_t$ (Figure 3b). $\langle PA_j \rangle_t$ produces trends consistent with $\langle QC_j^0 \rangle_t$, and $\langle QC_j^d \rangle_t$ does not depend strongly on the donor type (Figure 4). *Pathways* calculations are inexpensive compared to $\langle QC_j^d \rangle_t$ analysis, and conformational averaging is not needed for PA_j level analysis (although through-space decays do fluctuate with geometry).

Earlier studies show that extended-Hückel level tunneling currents do not strongly utilize hydrogen-bond mediation.²⁷ Because of the different treatment of numerical parametrizations in the extended-Hückel and *Pathways* models, it is difficult to judge which method best describes hydrogen-bond mediation. $\langle PA_j \rangle_t$ values provide a good approximation to extended-Hückel $\langle QC_j^d \rangle_t$ values in proteins when the *Pathways* hydrogen-bond decay factors are treated as through-space links. Nonetheless, the extended-Hückel-based score function provides a qualitatively correct description of the average protein decay factor $\beta/2$. The electronic propagation is quite sensitive to thermal fluctuations, and conformational averaging is essential to include in quantum calculation of T_{DA} . Because the *Pathways* analysis lacks explicit interferences among pathways, differences in static and dynamically averaged PA are not large. That is, the *Pathways* model for static structures approximates the score function of the conformationally averaged semiempirical quantum scores.

5. Conclusions

We used a conformationally averaged score function to describe the electronic propagation through proteins and water. Mappings of this kind may help to identify protein structure effects on inter- or intramolecular ET. The score function has a distance dependence consistent with experimental values in helical proteins and with the *Pathways* model. The electronic propagation through water decays very rapidly. The water result is not consistent with bulk water ET experiments. The mechanism of water-mediated superexchange at a protein interface can be different from ET through bulk water.⁶¹ ET at the protein interface is dominated by hole-mediated superexchange. The distance decay for the electronic coupling for electron-mediated superexchange through water is much smaller than that for hole-mediated superexchange through water.

Structures with strong quantum interferences form a small fraction of the protein ensemble and the significance of these weakly populated conformations is the subject of ongoing study. The extended-Hückel dynamically averaged score function for myoglobin is consistent with electronic couplings calculated with the *Pathways* model for static structures. Both *Pathways* and explicit conformationally averaged quantum methods produce similar electronic coupling predictions.

Acknowledgment. We thank Dr. Igor Kurnikov for his assistance with the HARLEM scripts. This research was supported by the National Institutes of Health (GM-048043) and by the VW Stiftung. Additional support from the NEDO Foundation (Japan) is gratefully acknowledged.

Appendix A

The two-state superexchange mechanism fails as E approaches resonance with bridge orbitals. The initial electronic wave function $\psi^{(i)}(E)$ (eq 10) has a large population beyond

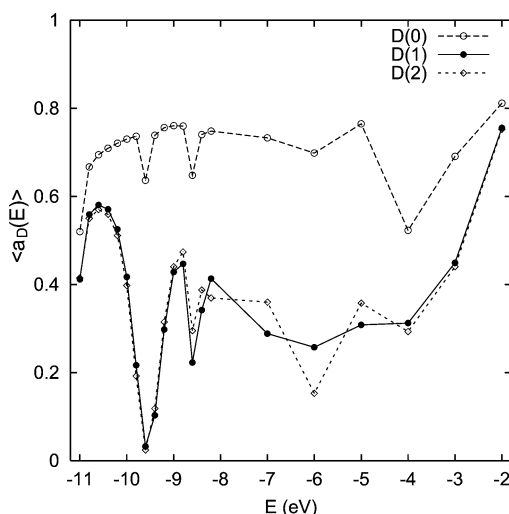


Figure 12. Root-mean-square deviation of the donor coefficient a_D in diabatic initial state over 200 MD snapshots. $\langle a_D \rangle \equiv \sqrt{1/N \sum_k a_D^2(t_k, E)}$. Three plot lines indicate different donor orbitals.

TABLE 2: LUMO and HOMO Energies for a Water Molecule and an Alanine Molecule at Extended-Hückel and Hartree-Fock (6-311++G(d,p) Basis Set) Levels^a

	molecular orbital energies (eV)			
	water		alanine	
	extended Hückel	HF/6-311++G(d,p)	extended Hückel	HF/6-311++G(d,p)
LUMO	0.3	1.2	-5.4	0.8
HOMO	-16.8	-13.8	-12.2	-11.4

^a Orbital energies for water at the extended-Hückel level are conformationally averaged. The alanine geometry is optimized with HF/6-311++G(d,p) analysis.

the donor ϕ_D as this resonance is approached. That is, a_D (eq 14) is small.⁴³ Figure 12 shows the root-mean-square value of $a_D(E)$ over 200 MD snapshots. a_D values for $D(1)$ and $D(2)$ are smaller than those for $D(0)$, because $D(0)$ localizes 90% and $D(1)$ and $D(2)$ localize 50% on the heme iron atom. Dips at -9.6 and -8.6 eV in Figure 12 indicate that $\psi^{(i)}(E)$ localizes on the Fe-N heme bonds (Figure 1). That is, QC_j^d indicates that the state remains localized on the heme, even though a_D in the Fe is small. Dips at -11.0 eV and at energies of the protein LUMO or above arise from resonances. Tunneling energies in this range are associated with possible hopping transport (based on the present extended-Hückel analysis).

Appendix B

Here, we explore the HOMO and LUMO energies for a water molecule and an alanine molecule at the extended-Hückel and HF levels. The alanine is used to examine the orbital structure of a peptide. These HF calculations are done using Gaussian98⁶³ with Table 2. In the tunneling energies close to the donor orbital energies (range of Figure 6a), the hole-mediated superexchange dominates the electronic coupling. The extended-Hückel calculation produces an alanine HOMO energy close to that computed with HF theory (less 1 eV difference). For high-energy electron transfer, the electron-mediated superexchange dominates the electronic coupling. The alanine LUMO at the extended-Hückel level is about 6.2 eV below the LUMO calculated at the HF level. The coupling decay factor, however, is insensitive to the choice of the tunneling energy.

The water HOMO energy at the extended-Hückel level is 3 eV lower than that at the HF level. The water HF calculation

gives a HOMO that is sensitive to the molecular geometry. That is, the hydrogen atomic orbitals contribute to the HOMO. In this case, hole-mediated superexchange can have slower coupling decay with distance than at the extended-Hückel level, because of the spatial distribution of the HOMO. The water LUMO energy at the extended-Hückel level is close to that found at the HF level.

References and Notes

- (1) Kawatsu, T.; Kakitani, T.; Yamato, T. *J. Phys. Chem. B* **2002**, *106*, 11356.
- (2) Balabin, I. A.; Onuchic, J. N. *Science* **2000**, *290*, 114.
- (3) Troisi, A. T.; Ratner, M. A.; Zimmt, M. B. *J. Am. Chem. Soc.* **2004**, *126*, 2215.
- (4) Troisi, A. T.; Nitzan, A.; Ratner, M. A. *J. Chem. Phys.* **2003**, *119*, 5782.
- (5) Daizadeh, I.; Medvedev, E. S.; Stuchebrukhov, A. A. *Proc. Natl. Acad. Sci. U.S.A.* **1997**, *94*, 3703.
- (6) Wolfgang, J.; Risser, S. M.; Priyadarshy, S.; Beratan, D. N. *J. Phys. Chem. B* **1997**, *101*, 2986.
- (7) Skourtis, S. S.; Balabin, I. A.; Kawatsu, T.; Beratan, D. N. *Proc. Natl. Acad. Sci. U.S.A.* **2005**, *102*, 3552.
- (8) Nishioka, H.; Kimura, A.; Yamato, T.; Kawatsu, T.; Kakitani, T. *J. Phys. Chem. B* **2005**, *109*, 1078.
- (9) Marcus, R. A.; Sutin, N. *Biochim. Biophys. Acta* **1985**, *811*, 265.
- (10) May, V.; Kühn, O. *Charge and Energy Transfer Dynamics in Molecular Systems*; Wiley-VCH: Berlin, 2003.
- (11) Medvedev, E. S.; Stuchebrukhov, A. A. *Chem. Phys.* **2004**, *296*, 181.
- (12) Prytkova, T. R.; Kurnikov, I. V.; Beratan, D. N. *J. Phys. Chem. B* **2005**, *109*, 1618.
- (13) Hopfield, J. J. *Proc. Natl. Acad. Sci. U.S.A.* **1974**, *71*, 3640.
- (14) Page, C. C.; Moser, C. C.; Chen, X.; Dutton, P. L. *Nature* **1999**, *402*, 47.
- (15) Larsson, S. *J. Phys. Chem.* **1984**, *88*, 1321.
- (16) Ponce, A.; Gray, H. B.; Winkler, J. R. *J. Am. Chem. Soc.* **2000**, *122*, 8187.
- (17) Miller, N. E.; Wander, M. C.; Cave, R. J. *J. Phys. Chem. A* **1999**, *103*, 1984.
- (18) Henderson, T. M.; Cave, R. J. *J. Chem. Phys.* **1998**, *109*, 7414.
- (19) Skourtis, S. S.; Beratan, D. N. *Adv. Chem. Phys.* **1999**, *106*, 377.
- (20) Beratan, D. N.; Onuchic, J. N.; Hopfield, J. J. *J. Chem. Phys.* **1987**, *86*, 4488.
- (21) Onuchic, J. N.; Beratan, D. N.; Winkler, J. R.; Gray, H. B. *Annu. Rev. Biophys. Biomol. Struct.* **1992**, *21*, 349.
- (22) Regan, J. J.; Onuchic, J. N.; *Adv. Chem. Phys.* **1999**, *107*, 467.
- (23) Langen, R.; Chang, I.-J.; Germanas, J. P.; Richards, J. H.; Winkler, J. R.; Gray, H. B. *Science* **1996**, *268*, 1733.
- (24) Beratan, D. N.; Betts, J. N.; Onuchic, J. N. *Science* **1991**, *252*, 1285.
- (25) Beratan, D. N.; Betts, J. N.; Onuchic, J. N. *J. Phys. Chem.* **1992**, *96*, 2852.
- (26) Jones, M. L.; Kurnikov, I. V.; Beratan, D. N. *J. Phys. Chem. A* **2002**, *106*, 2002.
- (27) Kawatsu, T.; Kakitani, T.; Yamato, T. *Inorg. Chim. Acta* **2000**, *300-302*, 862.
- (28) Okada, A.; Kakitani, T.; Inoue, J. *J. Phys. Chem.* **1995**, *99*, 2946.
- (29) Kuki, A.; Wolynes, P. G. *Science* **1987**, *236*, 1647.
- (30) Skourtis, S. S.; Beratan, D. N. *J. Phys. Chem. B* **1997**, *101*, 1215.
- (31) Gehlen, J. N.; Daizadeh, I.; Stuchebrukhov, A. A.; Marcus, R. A. *Inorg. Chim. Acta* **1996**, *243*, 271.
- (32) Cheung, M. S.; Daizadeh, I.; Stuchebrukhov, A. A.; Heelis, P. F. *Biophys. J.* **1999**, *76*, 1241.
- (33) Daizadeh, I.; Guo, J.-X.; Stuchebrukhov, A. A. *J. Chem. Phys.* **1999**, *110*, 8865.
- (34) Skourtis, S. S.; Regan, J. J.; Onuchic, J. N. *J. Phys. Chem.* **1994**, *98*, 3379.
- (35) Gruschus, J. M.; Kuki, A. *J. Phys. Chem. B* **1999**, *103*, 11407.
- (36) Aquino, A. J. A.; Beroza, P.; Regan, J.; Onuchic, J. N. *Chem. Phys. Lett.* **1997**, *275*, 181.
- (37) Liang, Z.-X.; Kurnikov, I. V.; Nocek, J. M.; Mauk, A. G.; Beratan, D. N.; Hoffman, B. M. *J. Am. Chem. Soc.* **2004**, *126*, 2785.
- (38) Liang, Z.-X.; Nocek, J. M.; Huang, K.; Kurnikov, I. V.; Beratan, D. N.; Hoffman, B. M. *J. Am. Chem. Soc.* **2002**, *124*, 6849.
- (39) Roitberg, A. E.; Holden, M. J.; Mayhew, M. P.; Kurnikov, I. V.; Beratan, D. N.; Vilkner, V. L. *J. Am. Chem. Soc.* **1998**, *120*, 8927.
- (40) Siddarth, P.; Marcus, R. A. *J. Phys. Chem.* **1990**, *94*, 8430.
- (41) Siddarth, P.; Marcus, R. A. *J. Phys. Chem.* **1993**, *97*, 2400.

- (42) Stuchebrukhov, A. A.; Marcus, R. A. *J. Phys. Chem.* **1995**, *99*, 7581.
- (43) Kawatsu, T.; Kakitani, T.; Yamato, T. *J. Phys. Chem. B* **2002**, *106*, 5068.
- (44) Katz, D. J.; Stuchebrukhov, A. A. *J. Chem. Phys.* **1998**, *109*, 4960.
- (45) Priyadarshy, S.; Skourtis, S. S.; Risser, S. M.; Beratan, D. N. *J. Chem. Phys.* **1996**, *104*, 9473.
- (46) Sumi, H.; Kakitani, T. *J. Phys. Chem. B* **2001**, *105*, 9603.
- (47) Smith, R. D. Correlations between Bound *N*-Alkyl Isocyanide Orientations and Pathways for Ligand Binding in Recombinant Myoglobins. Ph.D. Thesis, Rice University, 1999.
- (48) Bernstein, F. C.; Koetzle, T. F.; Williams, G. J. B.; Meyer, Jr., E. F.; Brice, M. D.; Rodgers, J. R.; Kennard, O.; Shimanouchi, T.; Tasumi, M. *J. Mol. Biol.* **1977**, *112*, 535.
- (49) Kalé, L.; Skeel, R.; Bhandarkar, M.; Brunner, R.; Gursoy, A.; Krawetz, N.; Phillips, J.; Shinozaki, A.; Varadarajan, K.; Schulten, K. *J. Comput. Phys.* **1999**, *151*, 283.
- (50) Howell, J.; Rossi, A.; Wallace, D.; Haraki, K.; Hoffmann, R. *QCPE* **1977**, *11*, 344 (FORTICON8).
- (51) Vela, A.; Gázquez, J. L. *J. Phys. Chem.* **1988**, *92*, 5688.
- (52) Kincaid, D. R.; Respass, J. R.; Young, D. M.; Grimes, R. G. *ITPACK 2C*; University of Texas: Austin, TX, 1999.
- (53) Oguni, T. *EIGRS*, version 1.2; updated in 1992. Oguni, T. *Gyoutetu Keisan (Matrix Calculation) Software*; Murata, K.; Miyoshi, T.; Dongarra, J. J.; Hasegawa, H., Eds.; Maruzen: Tokyo, Japan, 1999.
- (54) Kurnikov, I. V. *HARLEM*; 2002. <http://www.kurnikov.org/harlem> download.
- (55) Kaim, W.; Schwederski, B. *Bioinorganic Chemistry: Inorganic Elements in the Chemistry of Life*; John Wiley & Sons: New York, 1994; p 109.
- (56) *Iron Porphyrins, Part Two*; Lever, A. B. P., Gray, H. B., Eds.; Addison-Wesley Publishing Company: London, 1983.
- (57) Beratan, D. N.; Onuchic, J. N.; Hopfield, J. J. *J. Chem. Phys.* **1987**, *86*, 4488.
- (58) Gray, H. B.; Winkler, J. R. *Annu. Rev. Biochem.* **1996**, *65*, 537.
- (59) Gray, H. B.; Winkler, J. R. *Q. Rev. Biophys.* **2003**, *36*, 341.
- (60) Pitzer, R. M.; Merrifield, D. P. *J. Chem. Phys.* **1970**, *52*, 4782.
- (61) Lin, J.; Balabin, B. A.; Beratan, D. N. *Science* **2005**, *310*, 1311.
- (62) Humphrey, W. F.; Dalke, A.; Schulten, K. *J. Mol. Graphics* **1996**, *14*, 33.
- (63) Frisch, M. J.; Trucks, G. W.; Schlegel, H. B.; Scuseria, G. E.; Robb, M. A.; Cheeseman, J. R.; Zakrzewski, V. G.; Montgomery, J. A., Jr.; Stratmann, R. E.; Burant, J. C.; Dapprich, S.; Millam, J. M.; Daniels, A. D.; Kudin, K. N.; Strain, M. C.; Farkas, O.; Tomasi, J.; Barone, V.; Cossi, M.; Cammi, R.; Mennucci, B.; Pomelli, C.; Adamo, C.; Clifford, S.; Ochterski, J.; Petersson, G. A.; Ayala, P. Y.; Cui, Q.; Morokuma, K.; Malick, D. K.; Rabuck, A. D.; Raghavachari, K.; Foresman, J. B.; Cioslowski, J.; Ortiz, J. V.; Stefanov, B. B.; Liu, G.; Liashenko, A.; Piskorz, P.; Komaromi, I.; Gomperts, R.; Martin, R. L.; Fox, D. J.; Keith, T.; Al-Laham, M. A.; Peng, C. Y.; Nanayakkara, A.; Gonzalez, C.; Challacombe, M.; Gill, P. M. W.; Johnson, B. G.; Chen, W.; Wong, M. W.; Andres, J. L.; Head-Gordon, M.; Replogle, E. S.; Pople, J. A. *Gaussian 98*, revision A.11.3; Gaussian, Inc.: Pittsburgh, PA, 1998.